Full-Wave and Multi-GTD Analysis of the Ice Cloud Imager for MetOp-SG

Jakob Rosenkrantz de Lasson[1], Per Heighwood Nielsen[1], Cecilia Cappellin[1],
David Marote Alvarez[2], Marc Bergada[2], Raquel Gonzalez[2], Peter de Maagt[3]
[1]TICRA, Landemærket 29, DK-1119 Copenhagen, Denmark, jrdl@ticra.com
[2]Airbus/CASA, Avenida de Aragón 404, 28022 Madrid, Spain, david.marote@airbus.com
[3]European Space Agency (ESA/ESTEC), Keplerlaan 1, Noordwijk, The Netherlands, Peter.de.Maagt@esa.int

***Abstract*—We report an RF study at 50 GHz of the Ice Cloud Imager, consisting of a parabolic reflector inside a semi-closed sun shield, as obtained with full-wave method of moments (MoM) and the asymptotic high-frequency multi-geometrical theory of diffraction (Multi-GTD) method. The Multi-GTD results accurately reproduce details of the main beam and sidelobes originating from focusing, but fail to predict other parts of the pattern that are due to a large number of scattering events inside the semi-closed sun shield. MoM results at the half and double frequency (25 and 100 GHz) show that the parts of the pattern that are not well described by Multi-GTD, but still within the dynamic MoM range, remain at the same overall level as the frequency is varied. Thus, when analyzing at higher frequencies of interest ($\geq$ 183 GHz), a complementary MoM and Multi-GTD approach can be adopted to predict the radiation pattern.**

***Index Terms*—antenna, space, high frequency, scattering, MoM, Multi-GTD.**

I. Introduction

MetOp-SG is a cooperative undertaking between the European Space Agency (ESA) and EUMETSAT. The space segment of MetOp-SG consists of two series of satellites, the Satellite A and Satellite B series, providing weather data services to monitor the climate and improve weather forecasts.

The Ice Cloud Imager (ICI) will be mounted at the nadir platform of the MetOp-SG Satellite B and is intended to monitor cirrus clouds and cloud ice particles by means of brightness temperature retrievals. The ICI is a conical scanning microwave radiometer pointing at around 53° incidence angle, with several channels at frequencies between 183 and 664 GHz.

The instrument presents two different antenna systems and a hot calibration system within a single rotation. The three systems are: the main antenna, the cold sky antenna and the on-board calibration target system. The three systems share the same feed cluster, and only one of them is operative at a time depending on the rotation angle of the instrument. In this paper, we focus on the main antenna only, and an RF model of the ICI can be seen in Figure 1; we present the structure in more detail in Section II.

The purpose of the present paper is to report a comparative study of the RF performance of the ICI as obtained with full-wave MoM and the asymptotic Multi-GTD at 50 GHz. A detailed analysis of such a system at the ICI frequencies of operation would generally require the use of asymptotic high-frequency methods, where Multi-GTD is the most appropriate choice. However, the presence of a semi-closed sun shield enclosing the instrument makes the application of Multi-GTD particularly challenging. In order to estimate the accuracy of Multi-GTD for such a geometry, a comparison with a full-wave solution is thus necessary. A similar study was recently reported for the Planck telescope [1], showing excellent agreement between the two methods. Such a comparison is, however, not feasible at the high frequencies of the ICI, but is at 50 GHz. All computations are performed using the GRASP software tool [2] and associated MoM and Multi-GTD add-ons

The paper is organized as follows: In Section II, the ICI geometry is introduced in detail, while the computational methods are described in Section III. In Section IV, numerical radiation patterns are presented and discussed, in particular to compare MoM and Multi-GTD results and to investigate the effect of varying the frequency. Finally, Section V concludes the work.

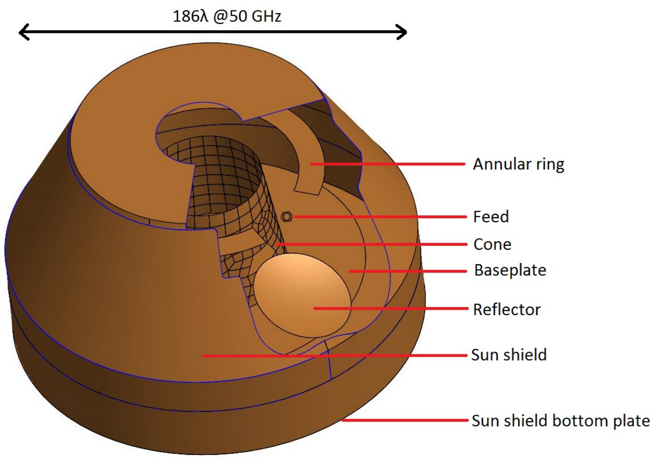

Fig. 1. ICI as analyzed in GRASP.

II. Geometry

The ICI, as analyzed in GRASP, is shown in Figure 1. It consists of a feed illuminating a parabolic reflector, and this system is enclosed in a sun shield with an opening to allow radiation to pass in the boresight direction of the reflector. Inside the sun shield, a partly open cone, which is supported by a baseplate, is included, and the feed is held in place by an annular ring. As shown in the figure, part of the annular ring has been removed close to the feed to avoid feed-scatterer proximity. The sun shield is closed by a circular plate at the bottom. In the actual system, a feed array is used, and the one feed used here is displaced by 4 mm from the main reflector focal point.

Selected dimensions of the structure are given in Table I. In GRASP, the full ICI structure is built from a large number of reflectors, scatterers, and plates for the Multi-GTD analyses, while for the MoM computations the largest part of the sun shield is imported as a CAD file.[1]

Part	Description	Size [mm]	Size [λ]
Main reflector	Aperture diameter	255	42.5
	Focal length	245	40.9
	Offset distance	212.5	35.4
Sun shield	Bottom diameter	1113	185.6
	Top diameter	699	116.6
	Conical part height	394	65.7
Baseplate	Diameter	924	154.1

TABLE I Selected dimensions of the ICI structure shown in Fig. 1. In the last column, $\lambda \simeq 6$ mm is the wavelength at 50 GHz.

Far-field patterns are reported in the coordinate system shown in Figure 2. The origin of the coordinate system is at the center of the main reflector and the z-axis (in blue) points towards the boresight of the reflector. The figure also displays examples of far-field cuts with $0° \leq \theta \leq 180°$ and $\phi = 0°, 90°, 180°$ and $270°$. Finally, all patterns are presented in linear polarization with co- and cross-polar components defined according to Ludwig's 3rd definition [3].

III. Computational methods

A. Method of moments

MoM is a full-wave technique that includes all reflection, scattering and coupling, and which thus, in principle, produces numerically exact results. The method is based on a surface integral formulation of Maxwell's equations with expansion of the unknown surface currents on a chosen set of basis functions. Once the currents have been computed, radiated far fields are obtained via radiation integrals. In GRASP, higher-order basis functions [4] augmented with a multi-level fast multipole method (MLFMM) adapted to such higher-order basis functions [5] give a highly efficient implementation for analyzing electrically large structures [6].

The accuracy of MoM results is limited by numerical discretization, and two important parameters that determine this accuracy are the expansion order of the polynomials to represent surface currents and the integration density of the radiation integrals. These parameters are controlled simultaneously in GRASP MoM with the Expansion Accuracy, whose default value is Normal.

[1]CAD export is already available in GRASP, while CAD import is under development and expected to be released with the next version of GRASP.

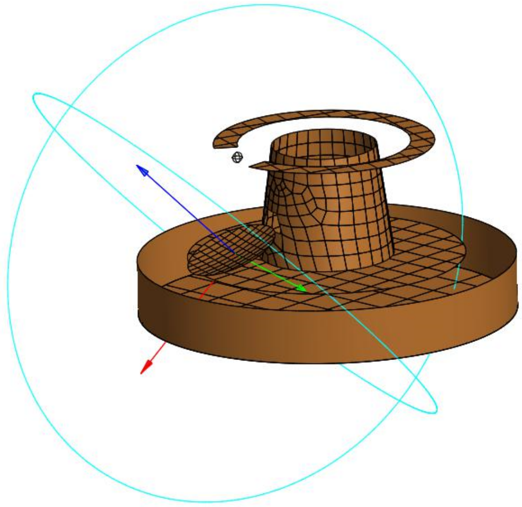

Fig. 2. Cut coordinate system, in which far-field patterns are reported. Examples of far-field cuts with $0° \leq \theta \leq 180°$ and $\phi = 0°$, $90°$, $180°$ and $270°$ are shown.

In Figure 3, we display the co-polar far-field pattern cut at $\phi = 0°$ for the ICI structure with Expansion Accuracy being either Normal (solid black) or Enhanced (dashed red). Enhanced corresponds to a higher polynomial order and a denser integration grid than Normal. It is apparent that the two patterns agree well down to approximately $65 - 70$ dBi under peak, and in the following sections Enhanced is used for all results. With this choice, we expect to have a dynamic range of approximately 65 dBi on the computed MoM patterns. In the region $10° \leq |\theta| \leq 90°$, the pattern exhibits a skirt-like shape, and given the dynamic range from above this is the part of the pattern that we determine accurately; other parts of the pattern ($|\theta| \geq 90°$) are at such low levels that they will be dominated by numerical errors.

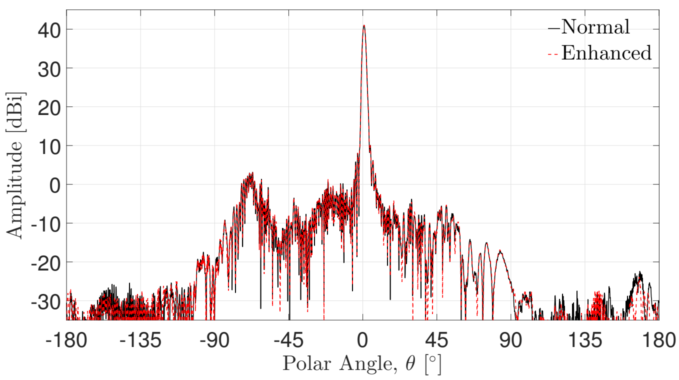

Fig. 3. MoM pattern cuts at $\phi = 0°$ with Expansion Accuracy as a parameter: Normal (solid black) and Enhanced (dashed red).

The MoM computations at 50 GHz were performed on a 48 CPU computer, required 108 GB of memory, and took ~ 9

hours. For an expected scaling with frequency squared [7], the MoM memory requirements at 183 GHz and 664 GHz would be ~ 1.5 TB and ~ 19 TB, respectively. Though time consuming, it is possible to supplement available RAM with storing directly on the harddisk using GRASP's built-in out-of-core solver [6].

B. Multi-geometrical theory of diffraction

Multi-GTD is a ray-tracing technique for describing the radiation from antenna systems and becomes increasingly accurate in the asymptotic high-frequency limit. In addition, it benefits from identification and interpretation of different contributions to the total pattern, which is absent when using MoM. With the Multi-GTD add-on to GRASP, fields due to selected scatterers are found by backward ray tracing. The zeroth order Multi-GTD field is the direct radiation from the feed, while the first order contribution stems from feed radiation that has been reflected or diffracted one time before going into the far field. Second-order contributions are reflected or diffracted rays that undergo a second scattering event before propagating into the far field.

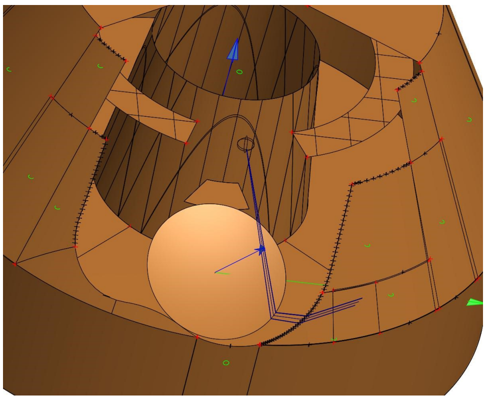

Fig. 4. Example of second-order Multi-GTD contribution.

As an example, Figure 4 illustrates a second-order Multi-GTD contribution due to diffraction at the main reflector edge and subsequently a second diffraction at the sun shield edge. The results reported in the following sections include Multi-GTD contributions up to fifth order. The development of such a model is an elaborate task, which requires a substantial amount of time, but once done the time and memory consumption for running the model is minimal compared to MoM, also at frequencies higher than 50 GHz.

As a final note, the field in caustic regions, such as the main beam, must be recalculated by physical optics (PO), which in these directions replaces the Multi-GTD field. Other caustics are detected from spikes in the individual ray path patterns and by keeping track of the number of ray traces generated for a given far-field direction.

IV. Numerical results

A. Feed

The feed used to excite the ICI has, in the $\phi = 0°$ cut, a co-polar pattern as shown in Figure 5 (in black). For comparison, a gaussian feed pattern is also shown (dashed red).

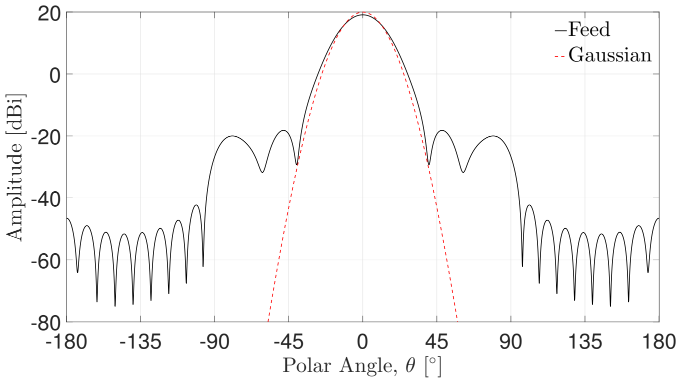

Fig. 5. Co-polar feed (solid black) and gaussian feed (dashed red) patterns in the $\phi = 0°$ cut. The gaussian has a taper of -20 dB at 24.91°.

B. MoM vs. Multi-GTD patterns

In Figure 6, we display the induced MoM surface currents on the ICI. As expected, a strong and tapered illumination of the main reflector as well as feed spillover around and below the reflector are seen. Moreover, a complex current distribution inside the sun shield is seen, which is due to multiple reflections inside the structure and to coupling between the surfaces.

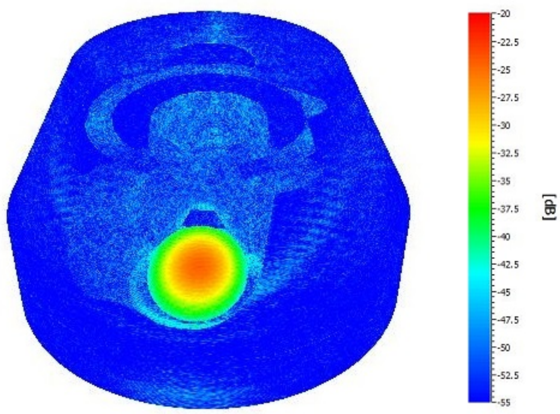

Fig. 6. MoM currents on ICI.

In Figure 7, we display 4π co-polar patterns obtained with MoM and Multi-GTD.[2] The main beam, located around $\theta = 0°$ and with a slight ϕ variation due to the offset of the feed from the paraboloid focal point, is practically identical in the

[2]Due to the available dynamic MoM range discussed in Section III-A and Multi-GTD limitations in predicting patterns behind the ICI, we focus on half of the 4π co-polar pattern, while the other half, the dark blue regions in Figure 7, is not analyzed.

two patterns. A region of relatively large field values around $\theta = 20°$ and $\phi = 180°$ is also visible in both patterns and stems, as shown by the Multi-GTD approach, from reflection and diffraction in the baseplate. Another common feature, that we return to below, is the large field around $\theta = 70°$ and $\phi = 180°$.

Having observed a couple of important quantitative and qualitative agreements between MoM and Multi-GTD, we also note substantial differences when considering finer details. While the Multi-GTD pattern exhibits a large number of distinct and sharp features, the MoM pattern is more smeared out, due to the high number of scattering and coupling events inside the semi-closed sun shield.

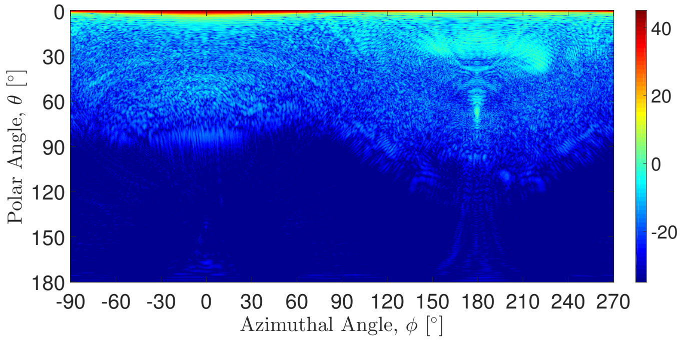

(a) MoM.

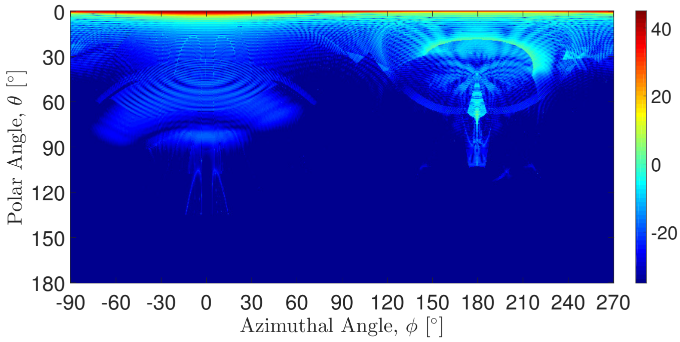

(b) Multi-GTD.

Fig. 7. MoM vs. Multi-GTD: 4π co-polar patterns as function of θ and ϕ.

In Figure 8, we compare the co-polar MoM and Multi-GTD pattern cuts for $\phi = 0°$ and $45°$. We observe excellent agreement in the main beam, while the relatively large sidelobe around $\theta = -70°$ in the $\phi = 0°$ cut is also well described by the Multi-GTD result (this sidelobe was seen around $\theta = 70°$ and $\phi = 180°$ in the pattern grids in Figure 7).

As illustrated for part of the structure in Figure 9, this sidelobe is due to feed spillover that reflects at the bottom and cylindrical walls of the sunshield and focuses in the far field. The cylindrical surface is singly-curved, so focusing in the far field is not as pronounced as upon reflection on the doubly-curved parabolic reflector. Early in the project, the baseplate radius was increased from 816 mm to the current 924 mm, and this partly blocked the feed spillover and reduced the sidelobe level from $\simeq 15$ dBi (not shown here) to the current level of $\simeq 3$ dBi.

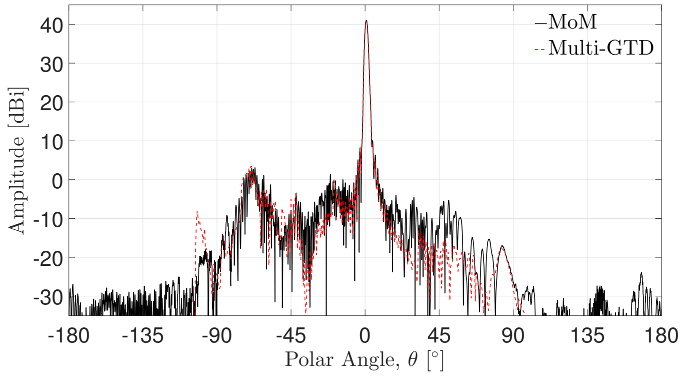

(a) $\phi = 0°$.

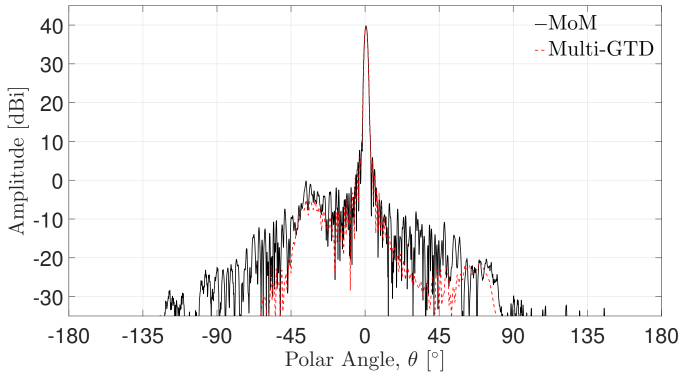

(b) $\phi = 45°$.

Fig. 8. MoM vs. Multi-GTD: Co-polar ϕ pattern cuts.

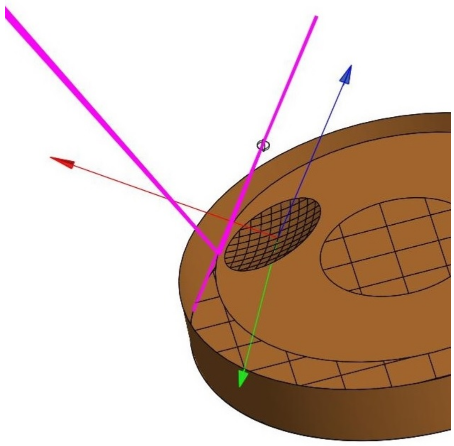

Fig. 9. Rays from the feed for part of the full structure, causing the high sidelobe around $\theta = -70°$ in Figure 8(a). The coordinate system is rotated by $\theta = -72.8°$ with respect to the one in Figure 2.

The MoM pattern exhibits, away from the main beam and the large sidelobe discussed above, a skirt-like shape (for $10° \leq |\theta| \leq 90°$). The Multi-GTD pattern consistently lies below this skirt and thus fails in predicting this part of the pattern accurately. However, as will be explained in the following section, it is possible to circumvent this limitation by making simultaneous use of the MoM results.

C. Frequency variation of MoM patterns

To assess the effect of varying the frequency, we have additionally computed the MoM radiation pattern at 25 and 100 GHz. In Figure 10, we compare the co-polar patterns at 50 GHz (black) with those at 25 (dashed red) and 100 (dotted blue) GHz in the $\phi = 0°$ and $= 45°$ cuts.

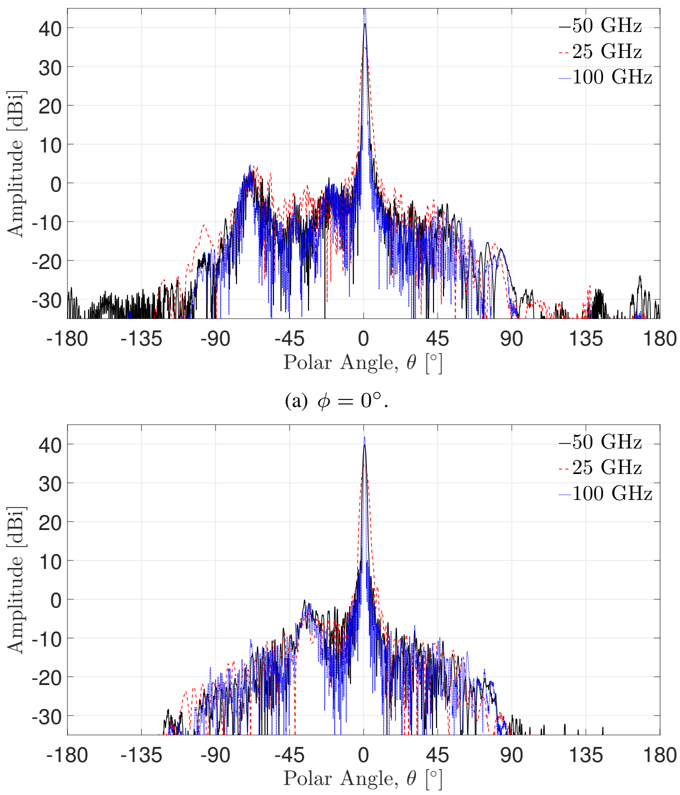

(a) $\phi = 0°$.

(b) $\phi = 45°$.

Fig. 10. MoM co-polar ϕ pattern cuts with frequency as parameter.

There are two main observations in this comparison. Firstly, the main beam directivity increases as expected by 6 dB when the frequency is doubled. Secondly, the skirt-like part of the pattern ($10° \leq |\theta| \leq 90°$) essentially remains at the same level when the frequency is varied. Based on these observations, we estimate that the skirt-like pattern will remain at the same level when the frequency is increased beyond 100 GHz, since this part of the pattern is largely due to multiple reflections and diffractions inside the sun shield, that do not provide any focusing in the far field. Therefore, its overall level remains constant as the frequency is varied. This is a key observation, since it implies that once we have computed the overall level of the skirt at a lower frequency, we will not need to compute it again at the higher frequencies. The main features of the radiation pattern (main beam and sidelobes due to focusing) can then, at the higher frequencies of interest, be computed accurately using a combination of Multi-GTD and PO, which is computationally feasible and accurate. If the details of the skirt-like pattern are needed at the higher frequencies, the comparison of MoM and Multi-GTD results at 50 GHz shows that this is not immediately possible; the Multi-GTD approach does not fully reproduce the MoM results, and a MoM solution is not currently feasible at ≥ 183 GHz.

V. Conclusion

We have compared RF simulation results, obtained with MoM and Multi-GTD at 50 GHz, for the Ice Cloud Imager that essentially consists of an offset reflector inside a semi-closed sun shield. The most important parts of the radiation pattern, i.e., the main beam and sidelobes due to focusing, agree well among the two approaches, while the skirt-like part around the main beam is underestimated by the Multi-GTD method. This skirt-like part of the pattern is due to a large number of scattering and coupling events inside the semi-closed sun shield, which is not captured by the Multi-GTD approach, unless an unfeasibly high number of orders is included. On the other hand, this part of the pattern was shown to remain at the same overall level as the frequency is increased. Therefore, in order to obtain a detailed pattern at the ICI frequencies of interest (≥ 183 GHz), a complementary and simultaneous use of MoM and Multi-GTD is suggested. More in detail, MoM is used at a lower frequency, i.e., at 50 GHz, in order to provide the skirt-like part of the pattern in the $10° \leq |\theta| \leq 90°$ range. Multi-GTD and PO are applied at the ICI frequencies to replace the pattern in the main beam and focusing sidelobe regions.

More generally, the analysis reported here show how MoM and Multi-GTD can be used simultaneously in order to complement each other and overcome their respective limitations when analyzing electrically very large and almost-closed structures. Multi-GTD is tailored for electrically very large structures, but becomes inaccurate for almost-closed geometries. MoM is accurate and exact for almost-closed structures but, even with the efficient higher-order basis functions and MLFMM implementation in GRASP, quickly becomes infeasible for electrically very large geometries.

References

[1] E. Jørgensen, P. H. Nielsen, O. Borries, and P. Meincke, "Full-wave modeling of the Planck telescope," in *36th ESA antenna workshop*, October 2015.

[2] GRASP Software, TICRA, Copenhagen, Denmark, www.ticra.com.

[3] A. Ludwig, "The definition of cross polarization," *IEEE Trans. Antennas Propag.*, vol. 21, no. 1, pp. 116–119, Jan 1973.

[4] E. Jørgensen, J. L. Volakis, P. Meincke, and O. Breinbjerg, "Higher order hierarchical Legendre basis functions for electromagnetic modeling," *IEEE Trans. Antennas Propag.*, vol. 52, no. 11, pp. 2985–2995, Nov 2004.

[5] O. Borries, P. Meincke, E. Jørgensen, and P. C. Hansen, "Multilevel fast multipole method for higher order discretizations," *IEEE Trans. Antennas Propag.*, vol. 62, no. 9, pp. 4695–4705, Sept 2014.

[6] E. Jørgensen, O. Borries, P. Meincke, M. Zhou, and N. Vesterdal, "New analysis capabilities for electrically large antennas and platforms," in *10th European Conference on Antennas and Propagation (EuCAP)*, April 2016.

[7] O. Borries, P. Meincke, E. Jørgensen, H.-H. Viskum, F. Jensen, and C. H. Schmidt, "Design and validation of compact antenna test ranges using computational EM," in *Proc. AMTA 37th Annual Meeting*, October 2015.